

Exploration of the stratosphere with cosmic-ray muons detected underground

C. Taricco ^{1,*} E. Arnone,¹ S. Rubineti,² and I. Bizzarri¹

¹*Department of Physics, University of Turin and Istituto Nazionale di Fisica Nucleare (INFN), Turin, Italy*

²*Department of Environmental Sciences, Informatics and Statistics, University Ca' Foscari of Venice, Venice, Italy*

N. Yu. Agafonova,¹ M. Aglietta,^{2,3} P. Antonioli,⁴ V. V. Ashikhmin,¹ G. Bari,⁴ G. Bruno,^{5,6} E. A. Dobrynina,¹ R. I. Enikeev,¹ W. Fulgione,^{5,3} P. Galeotti,^{2,3} M. Garbini,^{4,7} P. L. Ghia,⁸ P. Giusti,⁴ E. Kemp,⁹ A. S. Malgin,^{1,†} A. Molinaro,^{2,3} R. Persiani,⁴ I. A. Pless,¹⁰ O. G. Ryazhskaya,^{1,†} G. Sartorelli,⁴ I. R. Shakiryanova,¹ M. Selvi,⁴ G. C. Trinchero,^{2,3} C. F. Vigorito,² V. F. Yakushev,¹ and A. Zichichi^{4,7}

(LVD Collaboration)

¹*Institute for Nuclear Research, Russian Academy of Sciences, Moscow, Russia*

²*Department of Physics, University of Turin and Istituto Nazionale di Fisica Nucleare (INFN), Turin, Italy*

³*Istituto Nazionale di Astrofisica (INAF), Osservatorio Astrofisico di Torino, Turin, Italy*

⁴*University of Bologna and INFN, Bologna, Italy*

⁵*INFN, Laboratori Nazionali del Gran Sasso, Assergi, L'Aquila, Italy*

⁶*New York University Abu Dhabi (NYUAD), United Arab Emirates*

⁷*Centro Enrico Fermi, 00184 Roma, Italy*

⁸*Laboratoire de Physique des 2 Infinis Irène Joliot Curie, Centre national de la recherche scientifique (CNRS), 91406 Orsay, France*

⁹*University of Campinas, Campinas, Brazil*

¹⁰*Massachusetts Institute of Technology, Cambridge, Massachusetts, USA*



(Received 28 September 2021; accepted 1 February 2022; published 21 June 2022)

Cosmic radiation is a potential additional tool for atmospheric monitoring. High-energy cosmic rays, interacting in the atmosphere, produce secondary particles, the production and propagation of which are ruled by the state of the atmosphere. Atmospheric muons carry information on the stratosphere, as its temperature modulates their intensity. Here, we present a comprehensive investigation of the 24-year series of the muon flux recorded underground with the Large Volume Detector in the Gran Sasso Laboratory in Italy. Using advanced spectral-analysis methods, we reveal, in addition to the well-known annual cycle, two significant variations with periods of about four and ten years. These two multiannual components, however, are not present in the series of the so-called effective temperature—an average parameter commonly used to describe the entire atmospheric profile in relationship to the detected muon flux—but we find them in the series of the raw temperatures in the lower-stratospheric levels. We show that the weaker multiannual cycles emerge in the temperature series thanks to the dampening of the dominant annual radiative cycle at these levels, which are affected by higher-frequency variability related to transport and wave processes. We also show that the multiannual variations are not typical only of the Gran Sasso area but are present at large scales throughout the Northern Hemisphere. The analysis of the series of the muon flux also reveals evidence of daily to monthly scale variations, especially during the highly variable winter period. Although such short-term modulations are also found in the series of the effective temperature, we show that the variations of the two series are brought to better agreement when considering only specific layers of the atmosphere depending on the event. The amplitudes of the multiannual variations are significantly larger than those expected based on the temperature modulations. Such differences may be due to acknowledged difficulties of the adopted temperature reanalysis dataset to thoroughly represent long-term variability scales, so that long-term modulations in the raw temperature series and, consequently, in the effective temperature record would result as artificially attenuated. The muon flux therefore may be envisaged as a high time-resolution integrated proxy of lower-stratospheric temperatures.

DOI: [10.1103/PhysRevResearch.4.023226](https://doi.org/10.1103/PhysRevResearch.4.023226)

* carla.taricco@unito.it

† deceased

I. INTRODUCTION

The Earth's atmosphere, which shields the planet from most of the cosmic radiation, is in turn what allows us to measure at ground the most energetic cosmic rays via the phenomenon known as *extensive air showers*. Through successive interactions with the electrons and nuclei of atmospheric atoms and molecules, the showers convert the energy of the primary cosmic ray into many secondary particles (photons, electrons, positrons, hadrons, muons, and neutrinos) forming a cascade that develops toward Earth. Showers generated by high-energy cosmic nuclei may attain the maximum development near Earth and be thus measured in all their components. Instead, those engendered by the more numerous lower-energy primaries reach the maximum height in the atmosphere: the hadronic and electromagnetic components extinguish as the atmospheric depth increases, leaving only the longest-living particles, muons and neutrinos, to reach the Earth. Neutrinos and high-energy muons can even penetrate to great depths: the latter, thanks to their larger cross-section, can be more easily detected by underground experiments.

As the atmosphere is the vehicle of the shower development, its variable state must be considered when describing the observations of cosmic rays at ground. Pressure and temperature are the atmospheric parameters that most affect the rate and distribution of the different shower components, which in turn are differently affected depending on the nature of the particles. Also, the atmosphere layers that affect the shower evolution depend on the type of particles. Thus, while a change in pressure at ground, which corresponds to a change in the overburden matter, substantially modifies the electromagnetic component, it minimally affects the muonic one, which is more penetrating, the content of which is sensitive to temperature changes. The flux of higher-energy muons is influenced by the state of higher layers of the atmosphere (centered at ~ 100 hPa) because they are produced, in the early stages of the cascade, from the decay of unstable mesons (mostly charged pions, but also kaons), whose mean life is long enough so that they might re-interact before decaying.

The probability for the two processes depends on the density of the portion of atmosphere where the mesons propagate. When the temperature increases, the density decreases, and the competition between decay and interaction slightly changes in favor of decay, yielding more muons. Consequently, an expected feature of the muon flux measured underground is an annual modulation due to the seasonal temperature cycle in the stratosphere, the amplitude of which increases as higher-energy muons are sampled. The Large Volume Detector (LVD), which has been taking data since 1992 in the Gran Sasso Laboratory with the aim of detecting neutrinos from core collapse supernovae [1], is one of the deep underground instruments that has observed such a modulation (see Ref. [2] and references therein for measurements from other detectors). A Fourier-like spectral analysis of the LVD 24-y series of the muon flux, the longest one ever recorded, yielded evidence of the expected 1-y periodicity [2], well correlated with the variation of the so-called effective temperature, defined as the weighted average of the temperature at different levels of the stratosphere, with weights that are

larger for the levels where mesons are produced and decay into muons.

The harmonic analysis of the LVD muon-flux series hinted at the presence of additional subleading modulations, both at larger periods (of the order of several years) and at smaller ones (of the order of tens of days). Such variations seemed to be mostly unrelated to those of the effective temperature. These two cues call for a deeper investigation of the muon and temperature data. On the one hand, a more complex spectral analysis of the LVD muon-flux series is needed to conclusively determine all the components. This is one of the objectives of this paper. On the other hand, another goal of this paper is a more complex investigation of the effects of temperature variations on the muon flux, by considering the sources of variability in the different layers of the stratosphere.

In fact, the stratosphere, despite being stably stratified and with a typical radiative relaxation time of the order of 2 wk, shows a variability due to both radiative-driven and wave- and dynamically driven processes, the latter continuously driving its mean state away from radiative equilibrium especially during winter [3]. On the one hand, radiative-driven variability, which is dominated by the seasonal cycle induced by the orbital modulation of the solar irradiance, is also affected by longer-term variations in the solar flux (e.g., the 11-y solar cycle), which are large in its ultraviolet (UV) component. This modulation directly affects UV absorption by ozone and, consequently, stratospheric temperatures, with a peak amplitude of the order of 0.5–1.0 K, although several further indirect mechanisms come into play, as discussed in Ref. [4]. On the other hand, dynamically driven variability is particularly evident at mid and high latitudes largely due to planetary wave breaking and wave interaction with the polar jet. This variability is often manifested in terms of sudden stratospheric warmings (SSWs), whereby stratospheric temperatures show an abrupt increase accompanied by a reduction or reversal of westerly winds because of a disruption or displacement of the polar vortex [5]. Large SSWs can also impact weather conditions at the surface and drive weather patterns such as the negative phase of the North Atlantic oscillation [6]. Temperatures in the midlatitude upper troposphere are modulated not only by large-scale dynamics but also by synoptic weather systems, which can therefore project themselves onto the temperature. Both radiative-driven and dynamically driven processes in the stratosphere, which affect its temperature, can thus impact the muon flux by inducing complex variations.

The approach that we take in this paper consists of using advanced spectral methods, namely, the singular spectrum analysis (SSA) [7–10] and the wavelet transform coherence (WTC) [11,12], which allow for the extraction of all the significant components in the LVD muon-flux series and for the identification of the variability modes coherent with those characterizing the effective temperature time series. Moreover, to address the origin of the variations observed at periods other than 1 y, we apply the same methods not only to the series of the effective temperature but also to that of the temperatures at different layers in the stratosphere (from European Center for Medium-range Weather Forecast (ECMWF)

ERA-Interim [13]). The development of the work and its outcome are described here. After briefly introducing in Sec. II the relevant features of the muon and temperature data, the two spectral methods applied to their time series are shortly illustrated in Sec. III (and more in detail in Appendixes A and B), where we also show the results obtained in terms of the spectral content. In Sec. IV, we then focus on the long-term multiannual components and on their origin, while we discuss the short-term variability in Sec. V. The results of this paper are summarized in the concluding Sec. VI.

II. MUONS AND TEMPERATURE DATA

The LVD is a neutrino telescope conceived to monitor core-collapse supernova explosions in the galaxy. It is sited under about 1400 m of rock, in one of the three halls of the INFN Gran Sasso Laboratory (LNGS) (42.4275 °N, 13.5333 °E), at a minimal depth of 3100 m water equivalent. The detector, the dimensions of which are $13 \times 23 \text{ m}^2$ (footprint) and 10 m (height), is segmented into an array of 840 counters, which hold, in total, about 1000 tons of liquid scintillator. In each counter, the 1.2 tons of scintillator are viewed by three photomultipliers: the coincidence of the three signals in any counter determines the start of data collection. When this occurs, the amplitude and time of detection of the photomultiplier signals are acquired. To make sure to observe the neutrino burst associated to a gravitational collapse in the Milky Way—an event that occurs at an average rate of ~ 2 every 100 y—dedicated machine-learning software has been developed for the data acquisition to maximize the detector observation time, allowing the number of active counters to vary over time. Thanks to this treatment of its high modularity, LVD is operated with a duty cycle $\sim 100\%$.

Only a small fraction of the cosmic ray muons at sea level, 1 per million, have enough energy to penetrate down to the LNGS depth (the minimum energy, at the surface, for a muon to reach the LVD underground detector is 1.3 TeV). These muons can be easily recognized when passing through the LVD array, by inspecting the amplitude and time characteristics of the induced signals. The detector acceptance is calculated, on a time basis of 8 h, by means of a Monte Carlo simulation, to allow for the conversion of the time series of detected muons into that of the muon flux.

We use in this paper the same muon-flux time series (henceforth referred to as muon series) as in Ref. [2], where details are given on how it has been obtained. In short, it includes 5.48×10^7 muons registered from January 1994 to December 2017 over 8402 d, corresponding to $\sim 96\%$ of the total live time. The series comprises a few short (of the order of days) gaps. Also, two longer ones happened in 1996 (67 d) and in 2002 (24 d). As the analysis methods used in the following (see Sec. III) require the record to be homogeneous, here, we apply to the series a gap-filling procedure based on autoregressive (AR) models (see, e.g., [14]) with order estimated through the Akaike criterion [15]. The daily muon series is shown in Fig. 1(a) (red curve) in terms of relative deviations from the daily average, which is $I_\mu^0 = 3.35 \pm 0.0005^{\text{stat}} \pm 0.03^{\text{sys}} \times 10^{-4} \text{ m}^{-2} \text{ s}^{-1}$, consistent with other measurements obtained in the same laboratory (see Ref. [2] and references therein). The statistical uncertainties

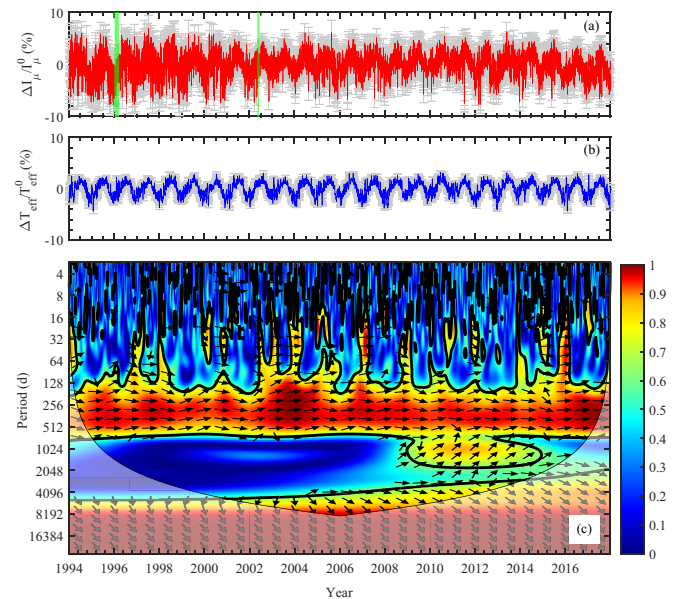


FIG. 1. (a) Percent variations of the daily muon flux $\Delta I_\mu/I_\mu^0$ and (b) of the daily effective temperature $\Delta T_{\text{eff}}/T_{\text{eff}}^0$ as a function of time. $I_\mu^0 = 3.35 \pm 0.03 \times 10^{-4} \text{ m}^{-2} \text{ s}^{-1}$ and $T_{\text{eff}}^0 = 220.3 \pm 0.5 \text{ K}$ are the daily mean of the flux and of the effective temperature, respectively [2]. The gray bars represent the statistical uncertainties. The sections highlighted in green in (a) represent the longer gaps in the muon flux time series, which happened in 1996 (67 d) and in 2002 (24 d), for which a gap-filling procedure was applied. (c) Wavelet transform coherence of the muon and effective temperature series. Areas with strongest (weakest) correlations are represented by the red (blue) color, respectively. The semitransparent area represents the cone of influence, while the black curves delimit the area in which the coherence is significant at 95% c.l. The relative phase-relation is shown as arrows: rightward for in-phase, leftward for antiphase.

are shown as gray bars, and the longer gaps in the series are highlighted in green. Note that, in this paper, in addition to the original daily muon series, we also exploit those rebinned in 5 d and monthly, which allows us to rather focus on long-term variability and to avoid redundancy related to high-frequency (daily scale) oscillations.

The variation of the muon flux in correlation with temperature changes in the upper atmosphere, where the muon production mostly happens, has been previously studied in Ref. [2]. Temperature data are from the ERA-Interim reanalysis dataset by the ECMWF [13], interpolated to the LVD location from its original $0.7^\circ \times 0.7^\circ$ grid. The adopted dataset consists of 4 values per day (one every 6 h) and is provided over 37 discrete pressure levels in the 1–1000 hPa range. To account for the fact that muons are not produced at a fixed pressure level, neither with fixed energy or direction, and as conventionally done for this kind of study, we incorporate those data into a unique effective temperature T_{eff} . Introduced in Ref. [16] and then developed in Refs. [17–19], it can be interpreted as the temperature of an ideal isothermal atmosphere that would produce the observed muon intensity. T_{eff} is obtained as a weighted average of the temperatures over the different atmospheric pressure levels. The weights account for the physics of production, propagation, and decay

of π and K mesons, being larger for pressure values at which the probability of decay into muons is larger. They exhibit a mild dependence on the product between the minimum energy required for the muon to reach a specific underground detector and its arrival direction, namely, the cosine of the zenith angle. This product is site dependent, and its average value has been evaluated for the muons detected in LVD in Ref. [2]. T_{eff} is then calculated as

$$T_{\text{eff}} = \frac{\sum_{n=1}^N \Delta X_n T(X_n) W(X_n)}{\sum_{n=1}^N \Delta X_n W(X_n)}, \quad (1)$$

where the index n runs over N pressure levels ($N = 37$ in our case). $T(X_n)$, $W(X_n)$, and ΔX_n are the temperature, the weight, and the thickness of the level X_n , respectively. The weights used for the calculation of T_{eff} are shown in Ref. [2]. By construction, T_{eff} is thus the quantity best describing the average effect of the atmospheric temperature variations on muons production. For high-energy muons, as those recorded by LVD, the changes of T_{eff} [20] have the dominant effect on the variation of the muon intensity. An effective temperature coefficient α_T can thus be defined as

$$\frac{\Delta I_\mu}{I_\mu^0} = \int_0^\infty dX_\alpha(X) \frac{\Delta T(X)}{T_{\text{eff}}^0} = \alpha_T \frac{\Delta T_{\text{eff}}}{T_{\text{eff}}^0}, \quad (2)$$

where $\Delta I_\mu/I_\mu^0$ and $\Delta T_{\text{eff}}/T_{\text{eff}}^0$ represent the relative deviations from the mean daily muon intensity and mean temperature, respectively. The value of α_T , obtained with a linear regression, is (0.94 ± 0.02) , the coefficient of correlation r , being $r = 0.56$ ($p_{\text{value}} < 10^{-5}$). The series of the daily effective temperatures is shown in Fig. 1(b) as a blue curve, in terms of relative deviations from the daily average, which is $T_{\text{eff}}^0 = 220.3 \pm 0.5$ K. The gray bars represent the statistical uncertainties.

In this paper, we still refer to the effective temperature, but mostly, we make use of the original temperature series at different pressure levels. Like for the muon data, we use daily, 5-d and monthly series of the temperature data. As expected, for the 5-d and 1-mo binning, the coefficients of correlation between muon flux and effective temperature are larger than for the 1-d binning, namely, $r = 0.72$ ($p_{\text{value}} < 10^{-5}$) and $r = 0.83$ ($p_{\text{value}} < 10^{-5}$), respectively. The study of the correlation coefficient between the muon and temperature series as a function of height, from 0 to 1000 hPa, is presented in Sec. IV.

III. SPECTRAL ANALYSIS

The study of the LVD muon series, as well as that of the effective temperature, has been performed in Ref. [2] by using a classical Fourier-like approach, namely, the Lomb-Scargle method [2,21]. However, in the presence of possible nonsinusoidal variations and for series with highly dynamical power range (i.e., including strong and weak spectral components), the Lomb-Scargle method is no longer the most appropriate tool. We thus use in the following advanced spectral methods which are suitable to efficiently extract and compare the deterministic components of the series under consideration. In this section, we first briefly describe the two complementary methods used in this paper, namely, the WTC and the SSA

(more details are given in Appendixes A and B, respectively). Then we present the results of the two methods applied to the muon and effective temperature series.

A. Methods

The WTC [11,12] allows for a multivariate analysis of time series. The advantage of this approach is related to the evolutionary characteristics of the wavelet methods, which allow one to efficiently reveal the amplitude modulation of the different variability components, as well as short-term events. Such methods are characterized by an accurate time resolution at high frequencies and by an accurate period resolution at low frequencies (see Appendix A). Specifically, in this paper, we first use the WTC to give a general view of the spectral features in common between the muon and T_{eff} series and to estimate their coherence over a broad range of periods, from days to decades.

We then deepen the analysis by applying the SSA to both series separately. This technique is designed to extract information from short and noisy time series [7–10]. It provides one with data-adaptive filters, which separate the time series into components that are statistically independent and that can be classified as oscillatory patterns and noise. The identified oscillations can be modulated in amplitude and phase. The statistical significance of the variability modes detected inside the records is assessed using a Monte Carlo test [10]. More information is given in Appendix B, while a complete description, as well as numerous applications, can be found in Refs. [8,22].

B. Results

The wavelet analysis, like other forms of evolutionary spectral analysis, offers an intuitive representation in a two-dimensional time-frequency plane, thus allowing one to visualize spectral content in common between the two series and to compare the common oscillations and their relative phase. The WTC method applied to the daily time series of the muon flux and of the effective temperature [see Figs. 1(a) and 1(b), respectively] results in the WTC spectrum illustrated in Fig. 1(c).

The broad red/yellow band surrounded by the black curve, extending over the entire time range between periods of ~ 128 to 512 d, indicates the highly significant correlation between the two series on an annual period, as expected. The alignment of the superimposed black eastward arrows over the entire period illustrates that the two series are also fully coherent, i.e., in phase. One can note two other high-correlation bands, in correspondence of periods of ~ 4 y (present with larger coherence from about 2008) and of ~ 10 y. For the latter, even if the wavelet spectrum also indicates some coherence of the two series, the red/yellow band lies for the most part outside the cone of influence (COI), i.e., in the region of the wavelet spectrum in which edge effects become important (see Appendix A). This indicates that the WTC method is not suitable to drive conclusions on such long-term components. This limitation does not affect the SSA method.

Finally, we notice an interesting feature revealed by this method. At the 30-d scale, along the whole period spanned

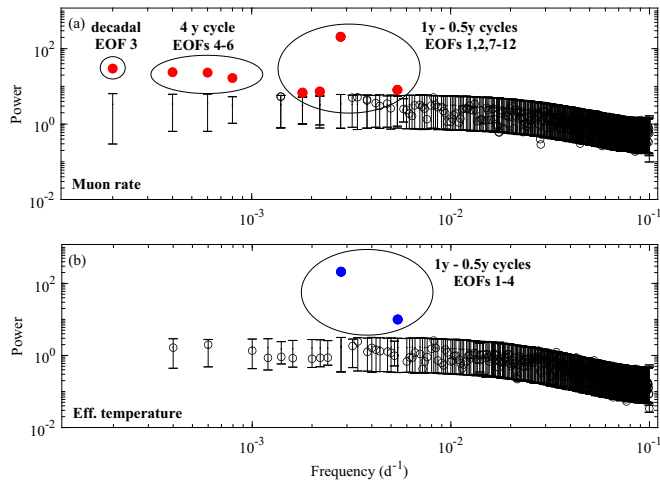


FIG. 2. (a) Monte Carlo singular spectrum analysis (SSA) results (99% c.l.) of the muon and (b) T_{eff} series. The Monte Carlo ensemble size is 10 000. The red (blue) dots highlight the spectral components included in the null hypothesis, while the empty ones indicate the spectral components that constitute the background, which can be parametrized as red noise (see text for details).

by the series, elongated power spots are evident (visible in yellow), corresponding to a coherent behavior of the two series. This significant feature appears to be localized in winter months, as one can evince by comparing the positions of the spots with the temperature behavior in Fig. 1(b), thus suggesting that sudden atmospheric phenomena characterizing the stratosphere [18] may be imprinted in the muon flux (see Sec. V).

The SSA is in turn applied separately to the time series of the muon flux and of the effective temperature rebinned in 5 d. This choice allows us to focus on long-term (annual and interannual) variability and to avoid redundancy related to high-frequency (daily-scale) oscillations. We adopt a window of width $W = M\Delta t = 2000$ d, where $M = 400$, and $\Delta t = 5$ d is the time resolution. We tested the robustness of the results for a wide range of M values (from $M = 300$ to 800).

The spectra of the two series are shown in terms of power vs frequency in Figs. 2(a) (muon flux) and 2(b) (effective temperature). A recursive procedure based on a Monte Carlo SSA test is designed to identify the statistically significant components present in the series [10]. Namely, we iteratively test, at a given confidence level, a set of null hypotheses, starting from the simplest one, the pure noise, up to more and more complex ones, including different combinations of spectral components superposed to the noise. To represent the noise, we assume an AR process of order 1 [AR(1) process] because it describes well the bias toward low frequencies, present in many time series, and it represents a suitable compromise between the excessive simplicity of white noise (e.g., Ref. [7]) and higher-order AR processes, which are themselves capable of oscillatory behavior [23]. The rejection of every null hypothesis is achieved by comparing the SSA spectrum of the analyzed time series with the Monte Carlo band, obtained by applying the SSA to an ensemble of 10 000 surrogate series generated by the considered model of the series (null hypothesis). Finally, the null hypothesis that cannot be rejected represents the model explaining the series and therefore

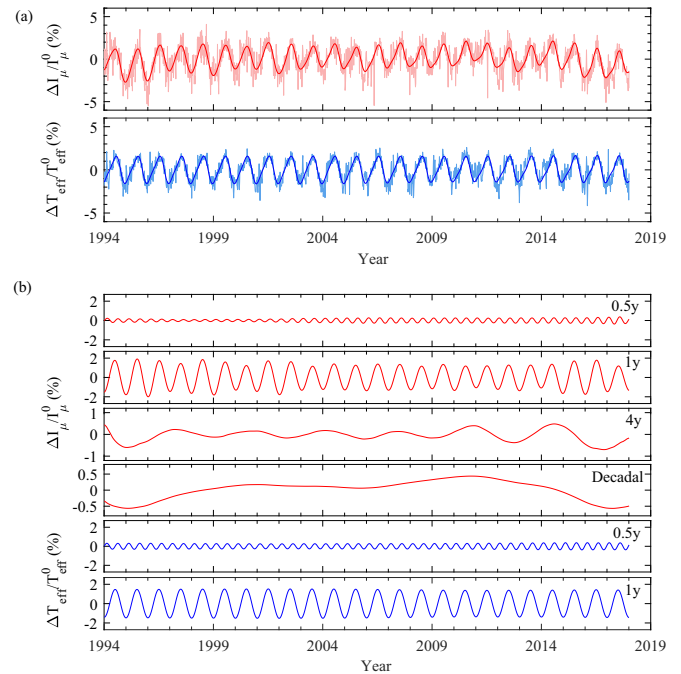


FIG. 3. (a) The reconstructed muon (red line) and T_{eff} (blue line) time series, given by the sum of the significant oscillations, superimposed on the corresponding 5-d series of muon (light red) and T_{eff} (light blue) data. (b) The significant (99% c.l.) singular spectrum analysis (SSA) components of the muon (red curves) and T_{eff} (blue curves) series. The decadal component is obtained by using a window width $M = 800$.

allows for the identification of the significant components at a given confidence level, which we choose to be 99%. In both panels of Fig. 2, the vertical bars, which bracket 99% of the power values obtained from the ensemble, represent the Monte Carlo band of the final step of the test procedure.

In the case of the muon series, the final step of the test, corresponding to the nonrejectable null hypothesis, is shown in panel (a) of Fig. 2. As one can see, no anomalous power exceeds the Monte Carlo band, except for those represented with red dots, associated to the components included in the null hypothesis, namely, a decadal trend component, and oscillations of 4-, 1-, and 0.5-y periods. Therefore, the model that includes these four components [empirical orthogonal functions (EOFs) 1–12; see Appendix B] and the AR(1) noise captures the variability of the muon flux series at 99% c.l. The noise represents 45% of the total variance: the denoised muon series resulting from the sum of the significant components is shown as a red line in Fig. 3(a), superimposed on the muon-flux data (light red).

Similarly, Fig. 2(b) shows the results of the same procedure applied to the series of the effective temperature: in this case, only two components, indicated with blue dots, exceed the Monte Carlo band, corresponding to 0.5- and 1-y periods. The model describing this record at 99% c.l. thus includes these two components (EOFs 1–4), superposed to the AR(1) noise. The noise in this case represents 30% of the series variance: the denoised effective-temperature series, obtained by summing the two significant components, is shown as a blue line in Fig. 3(a), superimposed on the data (light blue).

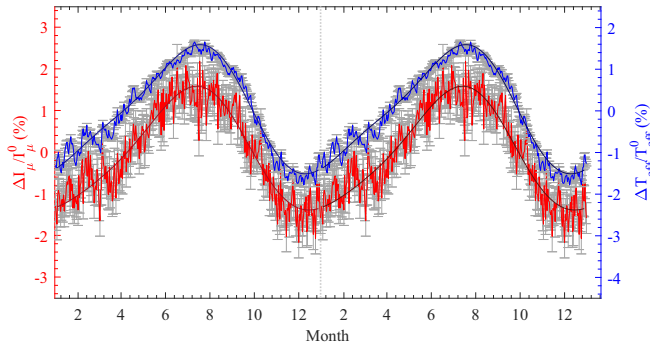


FIG. 4. Muon flux (red curve) and temperature (blue curve) daily series with the 24-y datasets folded onto a 1-y period. The light gray error bars correspond to the statistical uncertainties. The superposed heavy red and heavy blue curves correspond to the singular spectrum analysis (SSA) denoised signals [shown in Fig. 2(a)], similarly folded onto a 1-y period, for the muon-flux and effective-temperature series, respectively. The folded series have been duplicated to better visualize the minimum of the cycle during winter. The beginning of the duplicated series is indicated by the vertical gray-dashed line.

The reconstructed significant components detected in the two series are shown separately in Fig. 3(b). The red and blue curves pertain to the muon-flux and effective-temperature time series, respectively. One can see that the dominant variations in both series are the annual and semiannual components: for the muon-flux series, they explain about 46% of the total variance, while in the case of the effective-temperature series, they fully describe the variance related to the signal, which corresponds to 70% of the total variance. This dominant variability is the main cause of the high correlation between the two series ($r = 0.72$), which in fact becomes smaller ($r = 0.42$, $p_{\text{value}} < 10^{-5}$) for the annual/semiannual-detrended series.

The semiannual component is strongly related to the annual one and describes the pronounced asymmetry of the latter, due to the large temperature variability during winter, plausibly related to the occurrence of sudden warming events (as discussed in Sec. V). Such asymmetry is clearly visible in Fig. 4, where the two daily series of the muon flux (red curve) and the effective temperature (blue curve) are shown after folding the 24-y sequence onto a 1-y period. The thick superimposed curves correspond to the results of the SSA, which captures well such asymmetry [21].

A surprising result is that the multiannual components revealed in the muon series, accounting for $\sim 10\%$ of the total variance, have no counterparts in the effective-temperature series. Only a faint indication of the presence of a 4-y component in the T_{eff} series is found when applying the SSA to the monthly series and by decreasing the confidence level to 95%.

A deeper investigation of the multiannual components is the objective of the following section.

IV. MULTIANNULAR VARIATIONS: ORIGIN

As discussed in the previous section, the SSA of muon series, despite the high noise level (45% of the total variance) compared with that of the effective-temperature series

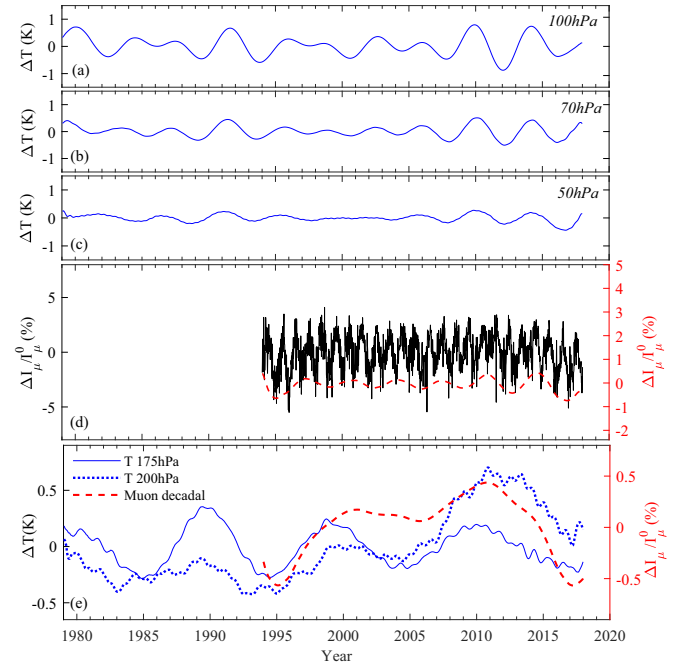


FIG. 5. The 4-y component revealed by the singular spectrum analysis (SSA) in the temperature series at (a) 100 hPa, (b) 70 hPa, and (c) 50 hPa. (d) 5-d muon series (black curve) and 4-y component (dashed red curve) revealed by the SSA. (e) The decadal component revealed by SSA in the 5-d muon series (dashed red curve) and in the temperature series at 175 and 200 hPa (blue curves).

(30%), yields an indication of a 4-y and a decadal modulation, capturing together $\sim 10\%$ of the total variance, in addition to the dominant annual component. In turn, such multiannual components are not present in the effective-temperature series. As variations in the muon flux must reflect temperature variations, we investigate the origin of such long-term components in the muon series by applying the SSA to the raw-temperature series, derived from the ECMWF reanalysis dataset (see Sec. II). We present the outcome of this analysis in Sec. IV A. We then discuss the relationship of the multiannual modulations with the dominant annual cycle in Sec. IV B, devoting Sec. IV C to considerations on the decadal variation in connection with the 11-y solar cycle.

A. SSA of the raw-temperature series

The SSA is applied to the raw-temperature series layer by layer. Moreover, given that the period covered by the ECMWF dataset extends from 1979 to 2018, we apply the analysis to the whole record, which allows us to explore more thoroughly the possible presence of long-term modulations. The complete set of results of the SSA of the raw-temperature series for the 21 different layers over the 1979–2018 period can be found in Table S1 in the Supplemental Material [24].

Concerning the 4-y component, it is detected in the low stratosphere. Its amplitude is maximum at ~ 100 hPa [Fig. 5(a)] and vanishes with altitude in the stratosphere [Figs. 5(b) and 5(c) corresponding to 70 and 50 hPa, respectively] and moving toward the troposphere. By comparing the detected component with that found in the muon series [shown

in Fig. 5(d) with a red curve], we find it in agreement in the last portion of the records, as already suggested by the WTC analysis [Fig. 1(c)].

As for the decadal modulation, it appears at ~ 175 hPa with the maximum amplitude and vanishes downward (see Table S1 in the Supplemental Material [24]). The reconstructed component (RC) is shown in Fig. 5(e) together with that at 200 hPa (blue curves). The comparison between these two components and that revealed in the muon series [Fig. 5(e), dashed red line] shows a remarkable agreement in shape, especially at 200 hPa. Precision is needed here on how the long-term temperature component at 200 hPa is determined.

The SSA of the 40-y temperature series, in fact, reveals a long-term trend in all layers, which as expected, shows the well-known temperature increase in the troposphere and the temperature decrease in the stratosphere (some of these trends are shown in Fig. S1 in the Supplemental Material [24]). The amplitude of these variations agrees with other findings (see, e.g., Ref. [25]).

The change of the slope of the temperature long-term trend occurs at ~ 125 – 200 hPa; because of the flatness of the trend at these levels, at 150 and 175 hPa, no significant trend variation is revealed (see the last column of Table S1 in the Supplemental Material [24]). However, while at 175 hPa the long-term variation of the temperature is fully described by the decadal oscillation, at 200 hPa, an additional trend component is needed to describe the variation. It is thus plausible that such a component is embedded also in the muon series, although its more limited duration does not allow us to detect it. Therefore, to consistently compare the long-term temperature variability at 200 hPa [dotted blue curve in Fig. 5(e)] with the muon decadal component, we sum the two (decadal and trend) temperature components. This enhances the agreement in shape between the decadal component of the temperature series at 200 hPa and of the muon series.

Moreover, we notice that the muons do not show any evident long-term trend, neither in the original series (Fig. 1) nor in the decadal variation [red line in Fig. 5(e)]. This is because the muon flux results from the integration of production at different heights, with greater weights right around the tropopause; this causes an attenuation of the trend because the temperature decreases above the tropopause and increases below. Therefore, the lack of a muon trend further confirms our analysis of the relationship between muon data and temperature of the individual layers.

As we have seen, the comparison between the muon multiannual components and the corresponding temperature variations reveals a good shape agreement but evidences a discrepancy regarding the amplitude. If we consider the decadal variation and the correlation found in Ref. [2], a $\Delta I_\mu/I_\mu^0$ amplitude of 1% should correspond to a $\Delta T_{\text{eff}}/T_{\text{eff}}^0$ of $\sim 1\%$, i.e., $\Delta T_{\text{eff}} \approx 2.3$ K. At the 175–200 hPa levels, the decadal temperature variation is of ~ 0.75 K [blue curves in Fig. 5(e)]. Considering that these layers contribute to ΔT_{eff} for only 9.3%, the resulting variation of 0.07 K is a factor of 30 less than expected based on the muon flux variation. An analogous evaluation for the 4-y components yields a factor of ~ 10 . These differences might highlight known difficulties of the adopted reanalysis dataset to correctly describe long-term

variations in stratospheric layers [13,26], which may result in a possible attenuation of long-term wave- and transport-driven modulations due, e.g., to changes in the assimilated global observing system and by the presence of time-varying biases in models and observations. Moreover, the assumption of a constant solar activity forcing (constant value of solar irradiance) in the underlying atmospheric model may also

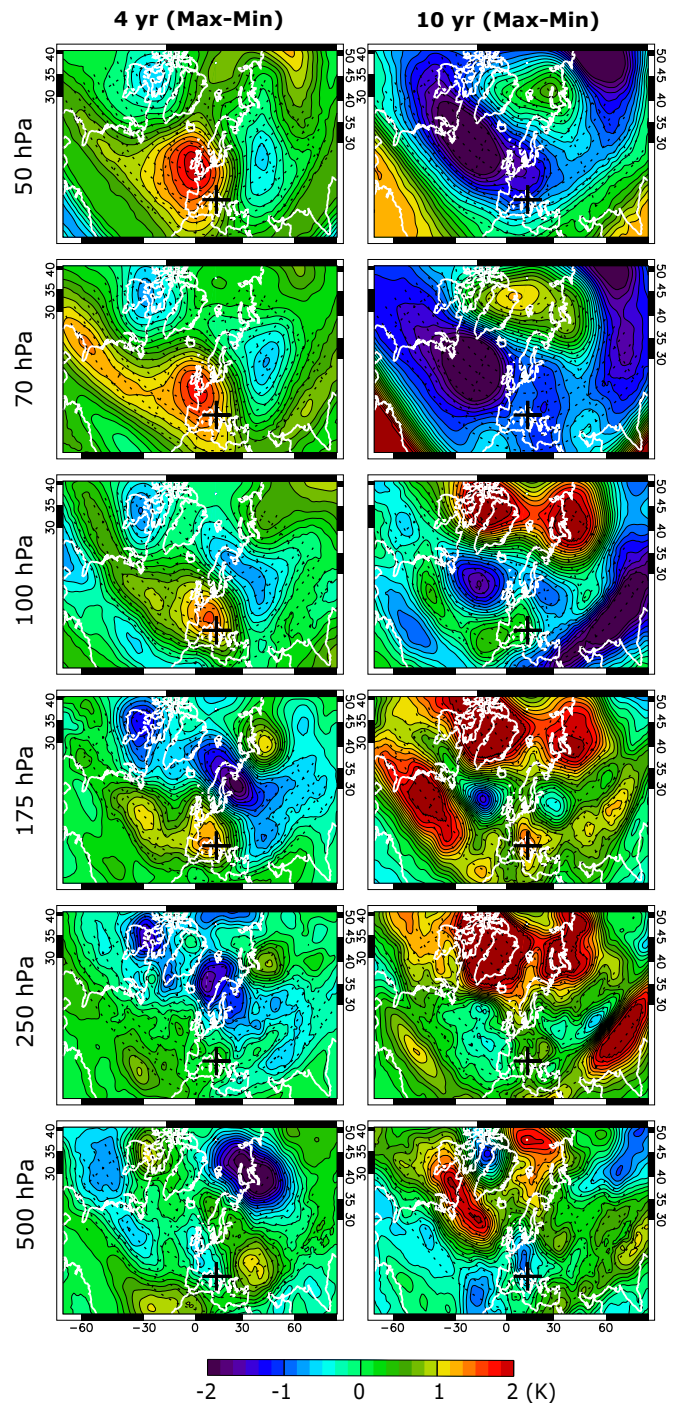


FIG. 6. Geographical distribution of temperature differences between years of maximum and minimum signal of the 4-y (left) and decadal (right) periodicity. Data are reported at significant (50–500 hPa) pressure levels for a large fraction of the Northern Hemisphere (see dashed meridians and parallels) with a focus on LNGS (black cross) and the polar region.

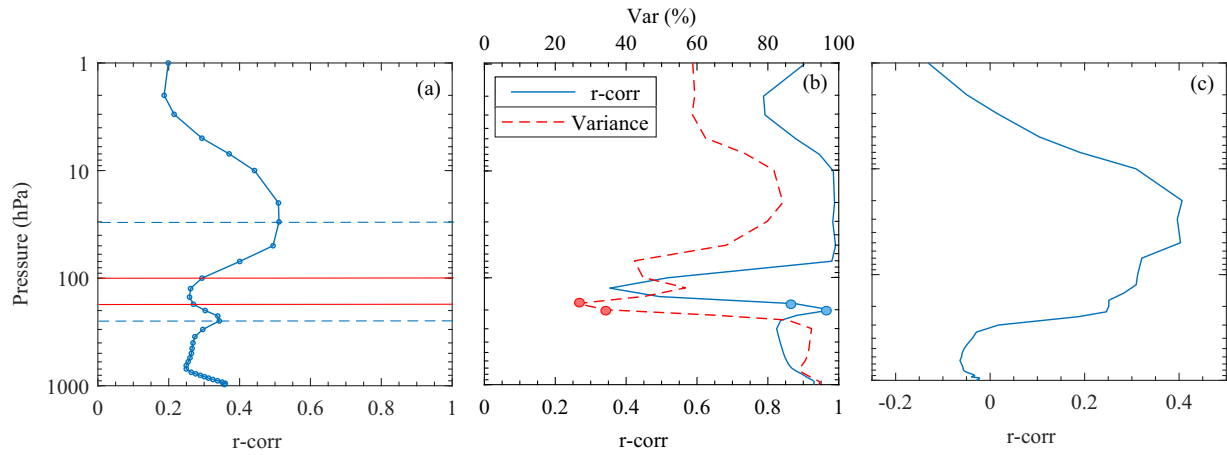


FIG. 7. (a) Correlation coefficient between muon and temperature daily data from 1 to 1000 hPa. The dashed blue lines mark the two correlation maxima, and the red lines identify the 100 and 175 hPa where the two multiannual periodicities have their maximum amplitude. (b) Correlation coefficient between the annual components of the temperature and muon series (blue curve) and percentage of the total variance of the annual temperature component (dashed red curve) from 1 to 1000 hPa. (c) Correlation coefficient between temperature and muon series after detrending them with the annual cycle determined with the singular spectrum analysis (SSA).

contribute to dampen the resulting decadal-scale temperature modulation.

These results refer to the Gran Sasso area. To put the findings in a larger-scale perspective, we consider the geographical distribution of temperature, under the form of temperature maps, over the Northern Hemisphere. We consider maps at specific pressure levels in three atmospheric regions: stratosphere, $> \sim 100$ hPa (selected levels: 50 and 70 hPa); upper troposphere–lower stratosphere, at and < 100 hPa, down to 250 hPa (100, 175, and 250 hPa); and troposphere, < 300 hPa (500 hPa).

To reveal the presence and the intensity of the 4-y and decadal oscillations at different levels, we show in Fig. 6 the maps of differences of temperature between maxima and minima for each periodicity. We identify these periods based on the SSA oscillations shown in Fig. 5.

We note that, in the layers suggested by the SSA (100 hPa for the 4-y and 175–200 hPa for the decadal oscillations) local maxima (indicated by the red features) are present. The 4-y component is also present at 70 and 50 hPa, as shown in Figs. 5(b) and 5(c), though the amplitude revealed by the SSA in these layers is smaller, possibly due to the dominance of the annual cycle at these heights, as shown in the next section. On the contrary, the decadal cycle is only present at 175–200 hPa and rapidly disappears above and below this layer. This analysis, in addition to confirming the results obtained by the SSA performed at different levels over the Gran Sasso region, shows that both cycles are not local, with the 4-y variation extending to several parts of Western Europe and the decadal variation being present at large scales throughout the Northern Hemisphere (Europe, North America, Atlantic Ocean, and high latitudes).

B. Relationship between multiannual components and annual cycle

The multiannual oscillations of the muon intensity thus result to be related to temperature variability near the tropopause

at 100 and 175–200 hPa levels. We explain the reason for this through a study of the correlation between muon and temperature series as a function of height.

We consider the correlation between the flux of muons and the temperature in the 37 atmosphere levels from 0 to 1000 hPa. The resulting correlation coefficient is shown in Fig. 7(a) as a function of pressure level. We note the presence of two local maxima centered at ~ 30 and 225 hPa (represented with

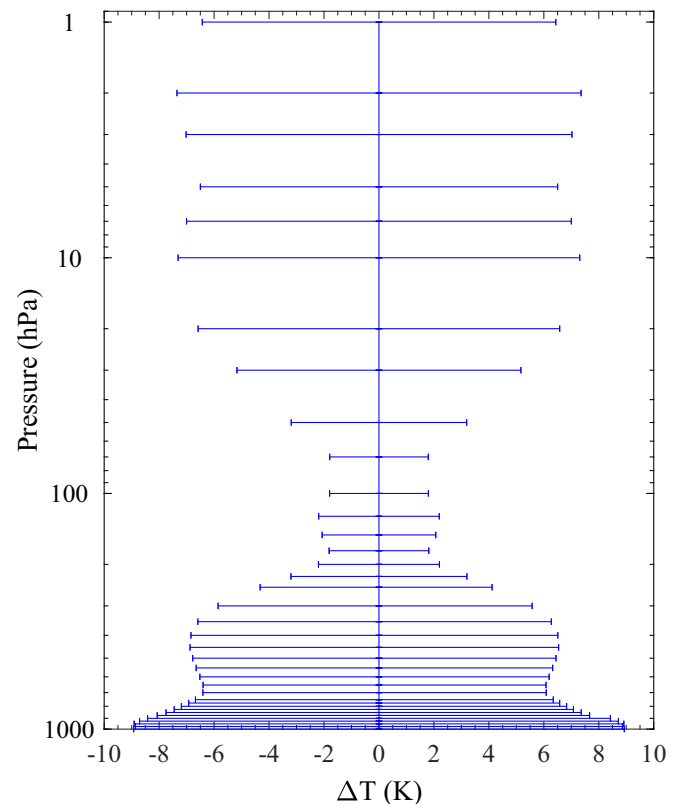


FIG. 8. Amplitude of the annual cycle, reconstructed by the singular spectrum analysis (SSA), from 0 to 1000 hPa.

the dashed blue lines), with a local minimum between 100 and 200 hPa (represented with red lines), around the tropopause. A similar behavior of the correlation coefficient as a function of height was found in Ref. [27]. It is interesting to remark that multiannual periodicities in the temperature series are revealed exactly in the layers around this minimum.

We make the hypothesis that the profile is mainly determined by the annual cycle, which is the dominant feature of the two series, and that the minimum of correlation is due to the weakening of this cycle. This is a plausible conjecture, given the dominant role of transport processes within this layer, which dampens the annual radiative modulation. To test our hypothesis, we first examine the average amplitude of the annual cycle (reconstructed by SSA) at different layers. This is shown in Fig. 8, from which one can note that the amplitude decreases by a factor of ~ 4 from 10 to 100–200 hPa and then increases again below this level.

Then we calculate the correlation coefficient between the annual components of the temperature and muon series as a function of the pressure level; this is presented in Fig. 7(b) (blue curve) together with the percentage of the total variance of the annual component of the temperature series (red dashed curve). The correlation coefficient shows a minimum around the tropopause, thus demonstrating that the minimum observed in the raw temperature series [Fig. 7(a)] is, in fact, related to the annual cycle. However, the minimum in Fig. 7(b) is sharper than that in Fig. 7(a); the correlation is remarkably high at 175 and 200 hPa, in contrast with what is observed in Fig. 7(a). The variance curve helps us to understand that, at these two levels, although the correlation is good, the amplitude of the annual component assumes the minimum value; moreover, we also notice that the annual temperature variance shows two minima at 100 and 175–200 hPa, just where the 4- and 10-y components were revealed.

Finally, we compute the correlation coefficient between temperature and muon-flux series after detrending them with the annual cycle determined with the SSA [Fig. 7(c)]; the characteristic shape with minimum at the tropopause disappears, confirming that it is determined by the annual cycle. Moreover, the correlation between the two series results to be significant at 100 hPa ($p_{\text{value}} < 10^{-5}$) and at 175 and 200 hPa ($p_{\text{value}} < 10^{-4}$), where it is supposed that the multiannual-scale temperature variations affect the muon series.

In conclusion, thanks to the attenuation of the dominant annual cycle at these levels, the weaker multiannual cycles emerge in the temperature series and in the muon series. To some extent, muons see better (weigh more) the same layers in which the annual cycle is attenuated. This demonstrates that the muon flux measured underground is particularly useful to reveal multiannual cycles because it results from the integration of production at different heights, with greater weights right around the tropopause.

C. Decadal muon component and the 11-y solar cycle

The presence of a decadal modulation in the muon series may suggest a relation with the 11-y solar cycle. While it is well known that cosmic rays with energies below tens of gigaelectronvolts are significantly anticorrelated with the 11-y

solar cycle, the muons they generate do not have enough energy to reach the Gran Sasso laboratory. In fact, at the location of the latter, the geomagnetic cutoff largely prevents these low-energy cosmic rays from even reaching the atmosphere. Moreover, even if additional muons, generated by low-energy atmospheric neutrinos interacting in the rock surrounding LVD, can contribute to the muon-flux decadal variation, the expected number is too small to explain the observed modulation. Therefore, we relate here the decadal cycle of the muon intensity with that of the stratospheric temperatures, which are in turn related to the 11-y solar cycle.

Indeed, stratospheric temperatures can be impacted by the 11-y solar cycle through direct or indirect mechanisms, resulting in peak amplitudes of the order of 0.5–1 K (2 K in particular regions; see a review in Ref. [4]). Solar UV variations can increase stratospheric temperatures through ozone absorption in the upper stratosphere, with enhanced meridional temperature gradients affecting the stratospheric jet and the Brewer-Dobson circulation. The modulation can then be projected onto surface weather patterns [6,28]. The reduced Brewer-Dobson circulation can also lead to warming of the equatorial lower stratosphere, which further alters the dynamics of the lower stratosphere. On the other hand, sea surface temperatures may be modulated through direct heating in the subtropics, with an amplification of the signal through enhancement of the Hadley and Walker circulations [29].

Because of the complexity of the mechanisms involved in projecting the 11-y solar cycle onto stratospheric temperatures, the temperature modulation is found at specific layers and regions, with large changes in sign and magnitude. Several studies involving both reanalysis data and global circulation models have identified an 11-y signal in the Northern Arctic region temperatures at ~ 10 hPa due to direct changes in the heating, extending to midlatitude and then connecting to a region at 100 to 20 hPa at low and midlatitudes due to indirect changes in the Brewer-Dobson circulation [28,30].

Because of these two regions of influence, the temperature in the Gran Sasso region is expected to show an imprint of the 11-y cycle in the low stratosphere, near the tropopause. This expectation is confirmed by the outcome of the SSA applied to the temperature series at different layers, which as discussed above, shows a decadal variation in the layer ~ 175 –200 hPa [blue curves in Fig. 9(c)], the shape of which is in agreement with the decadal one present in the muon-flux series [red curve in Fig. 9(a)]. We recall that the effective temperature does not show any decadal variability. It is interesting to note that a recent analysis of 10 y of data from the Borexino experiment [31], also situated in the Gran Sasso laboratory, shows the presence of a decadal modulation of the muon flux [Fig. 9(b)] in phase agreement with the last sunspot cycle [Fig. 9(e)]. Although only one decade is covered by the Borexino data (thus limiting the precision in determining an oscillation with a decadal period), the decadal trend is consistent with that found by SSA of the LVD data, as illustrated in Fig. 9(a), considering the different type of analysis performed.

Both temperature and muon-flux decadal variations replicate the 11-y solar cycle described by the sunspot time series. However, a phase misalignment between temperature and sunspots variations is apparent, with temperature maxima and minima anticipating those in the sunspot number.

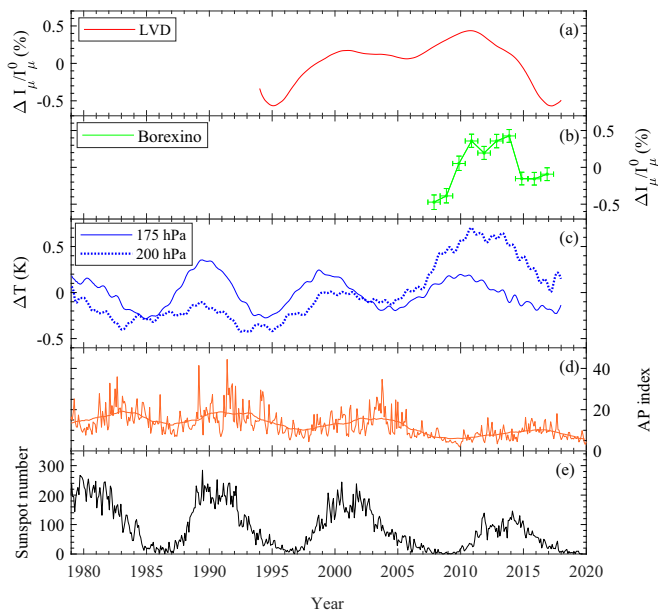


FIG. 9. (a) Singular spectrum analysis (SSA) decadal muon component from the Large Volume Detector (LVD) data, (b) Borexino muon-flux variation data, and (c) the SSA-decadal component revealed for temperature at 175 and 200 hPa (decadal plus trend components, dotted curve), (d) monthly mean Ap index (with superimposed running mean), and (e) total sunspot number. The SSA-decadal component of the atmospheric temperature has been obtained using a window width of $M = 180$ points (months) at 90% c.l.

An improved agreement may be found with the 11-y solar modulation of geomagnetic activity as recorded by the Ap index [Fig. 9(d)], which reaches its maxima in the descending phases of the 11-y sunspot cycle. Geomagnetic activity can affect stratospheric temperature by regulating energetic particle precipitation and their impact on atmospheric chemistry. The consequent temperature modulation can directly or indirectly depend on the region considered [32,33], so that the indirect correlation found between our measurements and the Ap index is not surprising. A further complexity arises due to the simultaneous action of the quasibiennial oscillation, which was found to amplify or reduce the effect of the 11-y cycle and geomagnetic activity on the stratosphere depending on its phase [4,32].

Such terrestrial effects modify the original solar signal imprinted in the stratospheric temperature, causing the nonperfect agreement between temperature (hence muon) variation and sunspot number series. Correctly interpreting the muon-temperature correlation at decadal scale will need further dedicated simulations, which go beyond the scope of this paper.

V. SHORT-TERM VARIABILITY COMPONENTS

The spectral analyses presented in Sec. III point to a correlation between the muon flux and the effective temperature also on shorter timescales, with consistent variations over days to weeks. On the one hand, the outcome of the wavelet coherence analysis [shown in Fig. 1(c)] indicates a significant correlation at scales of the order of 30 d or smaller, during the

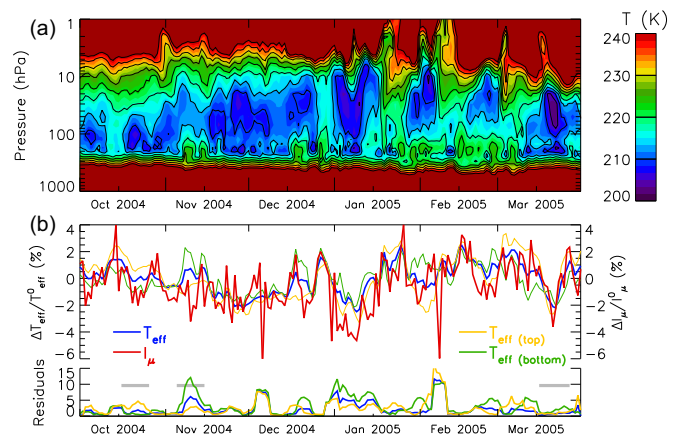


FIG. 10. Short-term variability in the 2004/2005 winter as depicted by time series of (a) temperature profiles at LNGS and (b) the comparison of daily T_{eff} (blue curve) and muon flux (red curve). (b) also shows T_{eff} evaluated considering only the top half of the weighting profile (<100 hPa) and the bottom half of it (green curve, > 100 hPa). The 5-d smoothed quadratic residuals of the time series of the three T_{eff} with respect to that of the muon flux are reported at the bottom of the panel. The horizontal gray bars identify the case studies adopted for Fig. 11 (March 2005) and for Figs. S2 and S3 in the Supplemental Material (October and November 2004) [24].

winter seasons. On the other hand, the SSA yields evidence of a semiannual modulation in both the series of the muon flux and the effective temperature [see Figs. 2(a) and 2(b), respectively]. This is, in fact, caused by the asymmetry of the annual modulation due to the observed large temperature variability during winter, which is well reflected in the muon-flux variation, as one can see from Fig. 4. In this section, we investigate more deeply such short-term variability, by extending the study of the muon-flux response to temperature variations in the different layers of the stratosphere, like we did in the previous section for the long-term modulations.

The agreement between short-term variations of the muon flux and the effective temperature is particularly evident, as noted above, during the winter period, which is highly variable, as in that season, the slowly changing radiative drive loses its predominance in favor of a dynamical variability. Dynamically driven variability indeed greatly affects the winter at mid to high latitudes in the Northern Hemisphere. A large source of short-term variability is the well-known phenomenon of SSW events, which are reflections of disturbances of the winter stratospheric vortex, with lower-latitude air masses entering the Arctic region and causing large temperature enhancements. Because of its geographical location, the effect on temperatures at the LNGS site can vary greatly from warming to cooling, depending on the actual geographical displacement or the disruption of the vortex. Several further short-term temperature variations occur due to dynamical internal variability and wave breaking in the midlatitude lower stratosphere and to variability in the upper troposphere related to synoptic weather systems.

A more in-depth example of the highly variable winter temperatures in the LNGS area is reported in Fig. 10 for the 2004–2005 cold season. The temporal evolution of temperature vertical profiles and how this is reflected in the time

series of T_{eff} and muon flux is shown in Figs. 10(a) and 10(b), respectively. Note that T_{eff} is contributed mostly by the 300–10 hPa layers (centered at ~ 100 hPa) and therefore reflects their variability. The top layers, between 50 and 10 hPa, have generally a marked variability, with several variations over a broad vertical extent lasting for 1 or 2 wk. These temperature changes are reflected in the behavior of T_{eff} and the muon flux, as one can see in Fig. 10(b). In turn, temperature enhancements in the bottom layers at ~ 200 hPa tend to last shorter and be much less deep, with a consequently less pronounced perturbation of T_{eff} . As we have found for the longer timescale variations, also for the short-scale ones, the amplitude of the variations of the muon flux are amplified with respect to that of T_{eff} , as one can see from Fig. 10(b) (red and blue curves), although at these timescales, this may be largely due to a smoothing effect of the coarser grid of the reanalysis data than the local character of the LVD signal. This behavior on short timescales is found in all winters that we have analyzed.

Notwithstanding the general agreement in shape between the variations of the two series, there are more or less pronounced discrepancies between them. The inspection of the temperature time series at various pressure levels shows that the agreement with the muon flux may be improved in several time periods when considering only a limited vertical portion of the atmosphere. For example, in Fig. 10(b), we report two additional T_{eff} series produced considering separately only the top half (< 100 hPa, T_{efftop}) or bottom half (> 100 hPa, $T_{\text{effbottom}}$) of the weighting profile. Some periods (e.g., in January 2005) show a qualitatively improved agreement when considering T_{efftop} calculated only on the top half of the atmosphere, pointing to a larger-scale dynamical forcing. On the contrary, in other periods (e.g., in October 2004), the agreement improves when considering only $T_{\text{effbottom}}$. The improvement tends to last for several days or weeks, so that it does not look to be due to a random effect, as confirmed by the inspection of the residuals, shown at the bottom of Fig. 10(b). A more complete analysis of further time intervals shows that there is not a fixed atmospheric layer that leads to improving the agreement between the T_{eff} and the muon-flux short-term variability but rather that a better agreement may be obtained by weighting into T_{eff} different portions of the atmosphere, depending on the perturbed conditions. Nevertheless, considering a fixed weighting profile, T_{eff} leads to the best agreement with the muon flux as compared with other choices. For example, over the 2004–2005 cold season, the square root mean deviation per day of T_{eff} , T_{efftop} , and $T_{\text{effbottom}}$ with respect to the muon flux is 0.109, 0.124, and 0.127, respectively, whereas it is 0.0189, 0.0199, and 0.0204 over the entire dataset.

To go further in the investigation, we examine the geographical distribution of temperature changes at different levels in the stratosphere. An example is shown in the two left columns of Fig. 11, where the temperature mean and variability (namely, the standard deviation) over the period January–March 2005 (JFM in short) are displayed at different pressure levels, in the first and second columns, respectively. As one can see, the mean and variability allow for the identification of different regimes in three regions: the stratosphere,

$> \sim 100$ hPa (first and second maps from the top), with large-scale dynamics related to the cold vortex centered over the Arctic region; the upper-troposphere–lower-stratosphere layer at and < 100 hPa down to 250 hPa (third to fifth maps), with the onset of variability on shorter spatial scales; and the tropospheric region, < 300 hPa (sixth maps), where the variability is locked to continental lands and increases moving closer to the surface. The different and more chaotic variability regime occurring in the middle layer clearly decouples from the large-scale dynamics, being a region known to be greatly affected by isentropic transport. This may explain the onset of the decennial component of the temperature modulation discussed in the previous section.

Figure 11 also shows, in the three last columns, the changes of the temperature during a case-study period over 16 to 27 March 2005, which corresponds to a sudden drop of the effective temperature, clearly visible in the time series shown in Fig. 10 (gray bar on the right). The identification of the three vertical regions aids in understanding the temperature changes during this period. The situation is typical of the passage of disrupted vortex-air directly above the LNGS area, with changes extending throughout a deep vertical portion of the atmosphere. In this case study, the vortex moves into its final warming stage, with a displacement from the Arctic and a split accompanied by a strong rotation (as depicted by potential vorticity maps, not shown) and replicated by the large-scale movement of cold and warm air masses (see the evolution from 16 to 27 March, e.g., at the 50 hPa pressure level, in the maps in the first row). In the upper stratosphere, the displacement and rotation lead to a tongue of air masses with high temperature over the LNGS site at the beginning of the event (16 March). The subsequent split of the vortex causes two regions of cold air to move over North America and central Europe, respectively (21 March). The latter induces the sudden drop of the temperature, as seen in the time series [Fig. 10(b)], with the largest changes in the 80–20 hPa layers, although a smaller-scale cold air mass can be identified down to 175 hPa. Also in these daily data, the maps in the middle layers show the change in regime, moving from large-scale variability of the upper layers to smaller scales and less organized structures, as depicted also by the JFM standard deviation. This change of regime between 100 and 250 hPa is consistent with the weakening of the annual cycle, described in Sec. IV B, which allows us to reveal the multiannual variations. At 250 hPa, the large-scale structures start to be influenced by the lower-tropospheric layers (see the 500 hPa layer), which then tend to lock to the continental lands closer to the surface (not shown). In this particularly deep event, both the muon flux and T_{eff} replicate well this sudden temperature drop.

This is a typical situation found at LNGS when dynamical changes, caused by a disrupted winter vortex (e.g., during SSWs), cause air masses to suddenly move above the LNGS site. When the perturbed conditions extend to a deep layer in the atmosphere, the consequent change of temperature leads to a synchronous change in the muon flux that can be more easily associated to the dynamical event. In this case, T_{eff} can describe well the overall impact of the stratosphere and upper troposphere onto the muon production. In the case of

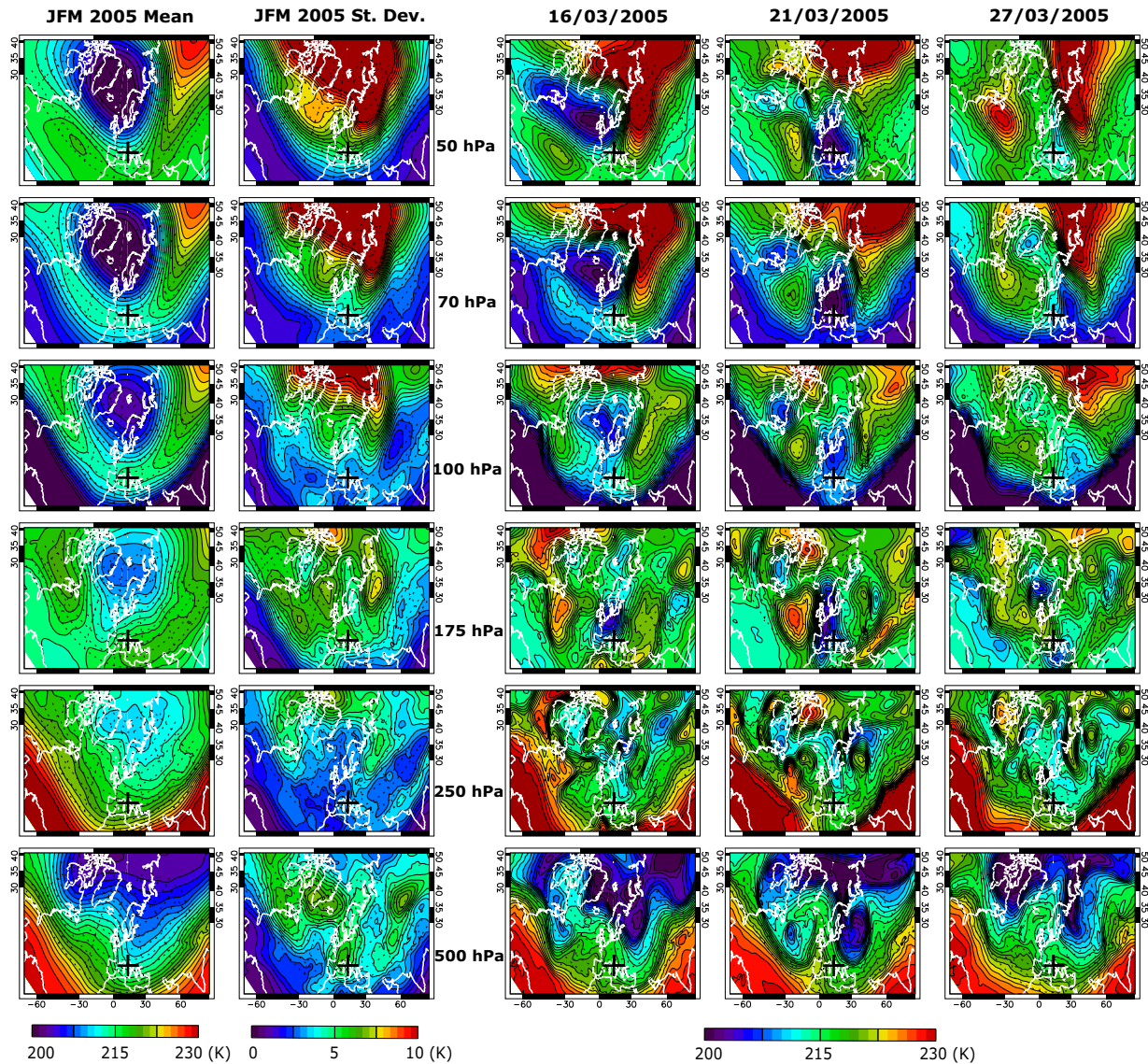


FIG. 11. Geographical distribution of temperature changes at significant (50 to 500 hPa) pressure levels over early 2005. Left columns: temperature mean and standard deviation over the period January to March (JFM) 2005. Right columns: daily temperature during 16 to 27 March 2005 [see gray bar in Fig. 10(b)]. Data are reported for a large fraction of the Northern Hemisphere (see dashed meridians and parallels) with a focus on LNGS (black cross) and the polar region.

less defined conditions (which typically decouple the 100–250 hPa layer), the changes in the muon flux seem to be affected more by specific layers and would suggest the need for weighting more a certain portion of the atmosphere (see further examples in the Supplemental Material, Figs. S2 and S3 [24]). The latter and similar situations are found also under the action of perturbations of the lower troposphere, then causing the much higher variability and less precise agreement found in the LNGS area as compared, for example, with other detectors more directly affected by vortex dynamics (see, e.g., Ref. [34]). In this sense, the agreement between the muon flux and effective temperature can be seen also as a meter of the ability to correctly describe and weigh temperatures at various atmospheric layers under several sources of variability; when the variability is highly inhomogeneous along the vertical profile, this ability can be greatly reduced.

Note that the analysis presented in this paper is based on ECMWF ERA-Interim global atmospheric reanalysis data [13], which although being based on a model, assimilates the largest available number of observations from a variety of instruments. To investigate the possible impact of the adopted dataset on our results, we also used NASA MERRA-2 Modern-Era Retrospective analysis for Research and Applications, Version 2 data [35]. A comparison over a short period was performed also with the ERA5 dataset [36]. We found that the difference when using different temperature datasets is negligible, both for single-layer temperature and in terms of T_{eff} , as compared with discrepancies between temperature data and the muon flux.

Finally, we must mention the shortages in the ability of the global models of these reanalysis datasets to correctly reproduce subgrid processes (e.g., gravity wave dispersion) that affect short-term variability in the upper troposphere and

stratosphere. This could also explain the difficulty to identify specific layers for the muon-temperature agreement on short timescales at the location of the LVD detector, as we did for long-term ones.

VI. CONCLUSIONS

The 24-y series of the flux of cosmic muons observed underground with LVD in the Gran Sasso Laboratory was analyzed using advanced spectral methods, namely, the WTC and the SSA. In addition to the well-known annual modulation of the muon intensity, we have revealed two multiannual components with periods of ~ 4 and 10 y. Differently from the annual periodicity, neither long-term component is present in the series of the effective temperature, a parameter commonly adopted to describe the temperature-driven variations of the muon flux. Instead, applying the SSA to the raw-temperature series from the ERA-Interim reanalysis dataset as a function of height, we have found that the temperature shows such multiannual oscillations in narrow vertical intervals near the tropopause, specifically at ~ 100 hPa for the 4-y and at 175–200 hPa for the decadal variations. We have determined that these oscillations, weaker than the annual one, emerge thanks to the dampening of the dominant annual radiative cycle at these levels, which are affected by higher-frequency variability related to transport and wave processes.

To generalize our findings, we have considered the geographical distribution of temperature over the Northern Hemisphere, showing that both multiannual cycles are not local features, as the 4-y variation extends to several parts of Western Europe, and the decadal variation is present at large scales throughout the Northern Hemisphere.

The analysis of vertically resolved temperature fields has allowed us also to detail variations observed on much shorter timescales, of the order of days to weeks. Short-term oscillations in the muon flux, found in the highly variable wintertime, generally trace variations of the effective temperature and reflect the dynamical evolution of air masses sounded by the muons in their journey through the atmosphere. The study of the geographical distribution of temperature changes in each layer shows, in turn, that the agreement between the two series largely depends on whether the changes occur homogeneously throughout the atmospheric depth. As expected from the local nature of their signal, muons manifest a larger sensitivity to short-term oscillations than the gridded temperature data, so that some local atmospheric perturbations seen by the muons may be missed by the temperature dataset.

As a concluding remark, we underline that the amplitude of the long-scale modulations imprinted in the muon series is much larger than those expected from temperature variations. The amplitudes of the 4-y and decadal modulations seen in the temperature series are, respectively, ~ 10 and 30 times smaller than those required to explain the amplitude of the corresponding oscillations observed in the muon series. These temperature variations of small amplitude make such a small contribution to the effective temperature that they are not significant in the spectrum of its series. All these results may conjecture difficulties of the adopted reanalysis dataset to correctly represent stratospheric temperature variability, with

a possible attenuation of long-term modulations in the raw-temperature series and in the effective temperature record. In turn, our analysis has shown that the intensity of muons underground is very sensitive to temperature variability in the lower stratosphere, suggesting that the measurement of variations in the muon flux may represent an additional high time resolution and unbiased integrated proxy of local stratospheric temperatures.

ACKNOWLEDGMENTS

The authors wish to thank all the staff of the INFN Gran Sasso Laboratory for their constant support and cooperation during all these years. Some of the scientists who imagined, realized, and contributed to the LVD experiment are not with us anymore. We are left with their memory and their teachings.

APPENDIX A

The Continuous Wavelet Transform (CWT) allows for an evolutionary spectral analysis of a series in the timescale plane [37,38]. The concept of scale is typical of this method; the scale is a time duration that can be properly translated into a Fourier period and hence into a frequency.

Given a finite-length sequence $X(n)$, the discretized CWT is defined as follows:

$$W_n^X(s) \approx \frac{1}{\sqrt{s}} \sum_{n'=0}^{N-1} X(n') \Psi_0^* \left(\frac{n' - n}{s} \right), \quad (\text{A1})$$

where Ψ_0 is the mother wavelet, s is the scale factor, and n is the lag.

The wavelet power spectrum gives a measure of the time series variance at each scale (period) and at each time and is defined as the absolute value squared of the wavelet transform.

Because one is dealing with finite-length time series, errors will occur at the beginning and end of the wavelet power spectrum. This issue is normally solved by zero-padding the signal, that is, by adding zeroes at the end of the time series before applying the wavelet transform. These added zeros constitute a signal discontinuity that influences the values of the CWT at both edges. Where this influence is present, the CWT values are modified with respect to their hypothetical true value (the one we could compute if we hypothetically had an infinite amount of data), and the larger the scale, the wider the time intervals adjacent to the edges in which the CWT is disturbed.

The width of these disturbed intervals is described by the COI at the considered scale. Therefore, the COI is the region of the wavelet spectrum in which edge effects become important; we take the COI as the area in which the wavelet power caused by a discontinuity at the edge has dropped to e^2 of the value at the edge.

To study the relative phase of the common oscillations, we applied the wavelet coherence methods.

Following Ref. [39], the wavelet coherence of two time series is defined as

$$R_n^2(s) = \frac{|S(s^{-1} W_n^{XY}(s))|^2}{S[s^{-1} |W_n^X(s)|^2] S[s^{-1} |W_n^Y(s)|^2]}, \quad (\text{A2})$$

where S is a smoothing operator, W^X is the wavelet transform of the time series, and $W^{XY} = W^X W^{Y*}$ is the cross wavelet transform of the two time series. This definition closely resembles that of a traditional correlation coefficient, and it is useful to think of the wavelet coherence as a localized correlation coefficient in time-frequency space.

We evaluated the spectra using the Paul wavelet with parameter $M = 4$. This wavelet is narrower in time than the Morlet wavelet, which is the mother wavelet generally applied, and this produces a better temporal localization of transient events.

The spectra are calculated using the wavelet coherence MATLAB package by Grinsted *et al.* [12].

APPENDIX B

The SSA of a time series of length N consists in three basic steps: embedding the time series in a vector space of proper dimension M (Refs. [7,8]), computing the $M \times M$ lag-covariance matrix C_D of the data [9], and diagonalizing C_D to yield the diagonal matrix $\Lambda_D = E_D^T C_D E_D$, where $\Lambda_D = \text{diag}(\lambda_1, \lambda_2, \lambda_3, \dots, \lambda_M)$, with $\lambda_1 > \lambda_2 > \lambda_3 > \dots > \lambda_M > 0$, and E_D is the $M \times M$ matrix having the corresponding eigenvectors E_k , $k = 1, M$ as its columns.

For each E_k , we construct the time series of length $N - M + 1$, called the k th principal component (PC), which

represents the projection of the original time series on the eigenvector E_k (also called EOF). Each eigenvalue λ_k gives the variance of the corresponding PC, and its square root is called the singular value. Given a subset of eigenvalues, it is possible to extract time series of length N by combining the corresponding PCs; these time series are called RCs and capture the variability associated with the eigenvalues of interest. The results of the SSA were obtained using the SSA-MTM Toolkit (see Refs. [8,40]).

To reliably identify the oscillatory components in a series, the Monte Carlo method (MCSSA) is used [10]. We assume a model for the analyzed time series (null hypothesis), and we determine the parameters using a maximum-likelihood criterion. Then a Monte Carlo ensemble of surrogate time series (size 10 000) is generated from the model, SSA is applied to each surrogate series, and data are projected onto the EOFs of the null hypothesis to test whether it is possible to distinguish the series from the ensemble. Since a large class of physical processes generate series with larger power at lower frequencies, we assume AR(1) noise in evaluating the significant oscillations. This is done to avoid overestimating the system predictability by underestimating the amplitude of the stochastic component of the time series [7]. The recursive procedure we designed to extract the deterministic components of the series is described in the text.

-
- [1] N. Y. Agafonova, M. Aglietta, P. Antonioli, V. V. Ashikhmin, G. Badino, G. Bari, R. Bertoni, E. Bressan, G. Bruno, V. L. Dadykin *et al.* (The LVD Collaboration), Implication for the core-collapse supernova rate from 21 years of data of the Large Volume Detector, *Astrophys. J.* **802**, 47 (2015).
- [2] N. Yu. Agafonova, M. Aglietta, P. Antonioli, V. V. Ashikhmin, G. Bari, G. Bruno, E. A. Dobrynina, R. I. Enikeev, W. Fulgione, P. Galeotti *et al.* (The LVD Collaboration), Characterization of the varying flux of atmospheric muons measured with the Large Volume Detector for 24 years, *Phys. Rev. D* **100**, 062002 (2019).
- [3] G. P. Brasseur and S. Solomon, *Aeronomy of the Middle Atmosphere: Chemistry and Physics of the Stratosphere and Mesosphere* (Springer Science & Business Media, Dordrecht, 2005), Vol. 32.
- [4] L. J. Gray, J. Beer, M. Geller, J. D. Haigh, M. Lockwood, K. Matthes, U. Cubasch, D. Fleitmann, G. Harrison, L. Hood *et al.*, Solar influences on climate, *Rev. Geophys.* **48**, RG4001 (2010).
- [5] D. G. Andrews, J. R. Holton, and C. B. Leovy, *Middle Atmosphere Dynamics* (Academic Press, New York, 1987).
- [6] M. Baldwin and T. Dunkerton, Stratospheric harbingers of anomalous weather regimes, *Science* **294**, 581 (2001).
- [7] R. Vautard, P. You, and M. Ghil, Singular-spectrum analysis: a toolkit for short, noisy chaotic signals, *Physica D* **58**, 95 (1992).
- [8] M. Ghil, M. R. Allen, M. D. Dettinger, K. Ide, D. Kondrashov, M. E. Mann, A. W. Robertson, A. Saunders, Y. Tian, F. Varadi, and P. Yiou, Advanced spectral methods for climatic time series, *Rev. Geophys.* **40**, 3-1 (2002).
- [9] R. Vautard and M. Ghil, Singular spectrum analysis in nonlinear dynamics, with applications to paleoclimatic time series, *Physica D* **35**, 395 (1989).
- [10] M. R. Allen and L. A. Smith, Monte Carlo SSA: detecting irregular oscillations in the presence of colored noise, *J. Clim.* **9**, 3373 (1996).
- [11] C. Torrence and G. P. Compo, A practical guide to wavelet analysis, *Bull. Am. Meteorol. Soc.* **79**, 61 (1998).
- [12] A. Grinsted, J. C. Moore, and S. Jevrejeva, Application of the cross wavelet transform and wavelet coherence to geophysical time series, *Nonlin. Proc. in Geophys.* **11**, 561 (2004), freely available at <http://www.glaciology.net/wavelet-coherence>.
- [13] D. P. Dee, S. M. Uppala, A. J. Simmons, P. Berrisford, P. Poli, S. Kobayashi, U. Andrae, M. A. Balmaseda, G. Balsamo, P. Bauer *et al.*, The ERA-Interim reanalysis: configuration and performance of the data assimilation system, *Q. J. R. Meteorol. Soc.* **137**, 553 (2011).
- [14] S. M. Kay, *Modern Spectral Estimation: Theory and Application* (Pearson Education India, Bangalore, 1988).
- [15] H. Akaike, Fitting autoregressive models for prediction, *Ann. Inst. Stat. Math.* **21**, 243 (1969).
- [16] P. H. Barrett, L. M. Bollinger, G. Cocconi, Y. Eisenberg, and K. Greisen, Interpretation of cosmic-ray measurements far underground, *Rev. Mod. Phys.* **24**, 133 (1952).
- [17] M. Ambrosio, R. Antolini, G. Auriemma, R. Baker, A. Baldini, G. C. Barbarino, B. C. Barish, G. Battistoni, R. Bellotti, C. Bemporad *et al.* (MACRO Collaboration), Seasonal variations in the underground muon intensity as seen by MACRO, *Astropart. Phys.* **7**, 109 (1997).
- [18] P. Adamson, C. Andreopoulos, K. E. Arms, R. Armstrong, D. J. Auty, D. S. Ayres, C. Backhouse, J. Barnett, G. Barr, W. L. Barrett *et al.* (MINOS Collaboration), Observation of muon intensity variations by season with the MINOS far detector, *Phys. Rev. D* **81**, 012001 (2010).

- [19] E. W. Grashorn, J. K. de Jong, M. C. Goodman, A. Habig, M. L. Marshak, S. Mufson, S. Osprey, and P. Schreiner, The atmospheric charged kaon/pion ratio using seasonal variation methods, *Astropart. Phys.* **33**, 140 (2010).
- [20] Note that the effective temperature is calculated independently for the four ECMWF datasets available for each day. The four values are then averaged, and their variance, typically 0.5 K, is used to estimate the uncertainty on the mean value.
- [21] The SSA-based description of the annual oscillation of the two series, more appropriate than the classical sinusoidal one, allowed us to accurately determine the amplitude and position of the maxima and minima on a year-by-year basis [2].
- [22] M. Ghil and C. Taricco, Advanced spectral-analysis methods, in *Proceedings of the International School of Physics "Enrico Fermi", Varenna on Lake Como, 1996*, edited by G. Castagnoli, and A. Provenzale (IOS Press, Amsterdam, 1997), Vol. 133, pp. 137–159.
- [23] Considering the time resolution of the series rebinned in 5 d as used here, the choice of AR(1) noise is consistent with the findings of the careful analysis of the noise given in Ref. [2].
- [24] See Supplemental Material at <http://link.aps.org/supplemental/10.1103/PhysRevResearch.4.023226> for trends revealed by SSA in atmospheric temperature time series, additional short-term case studies of the temperature geographical distribution, and variance of the significant SSA-components of the atmospheric temperature at different levels, of the muon flux and of the effective temperature.
- [25] A. K. Steiner, F. Ladstädter, W. J. Randel, A. C. Maycock, Q. Fu, C. Claud, H. Gleisner, L. Haimberger, S.-P. Ho, P. Keckhut *et al.*, Observed temperature changes in the troposphere and stratosphere from 1979 to 2018, *J. Clim.* **33**, 8165 (2020).
- [26] A. Simmons, C. Soci, J. Nicolas, B. Bell, P. Berrisford, R. Dragani, J. Flemming, L. Haimberger, S. Healy, H. Hersbach *et al.*, *Global Stratospheric Temperature Bias and Other Stratospheric Aspects of ERA5 and ERA5.1*, (European Centre for Medium-Range Weather Forecasts, Reading, 2020), Technical Memo 859.
- [27] V. B. Petkov, M. G. Kostyuk, R. V. Novoseltseva, Y. F. Novoseltsev, L. V. Volkova, P. S. Striganov, and M. M. Boliev, Temperature variations of high energy muon flux, in *Proceedings of the 32nd International Cosmic Ray Conference (ICRC, Beijing, 2011)*, Vol. 11, pp. 386–389.
- [28] L. J. Gray, A. A. Scaife, D. M. Mitchell, S. Osprey, S. Ineson, S. Hardiman, N. Butchart, J. Knight, R. Sutton, and K. Kodera, A lagged response to the 11-year solar cycle in observed winter Atlantic/European weather patterns, *J. Geophys. Res.: Atmos.* **118**, 13405 (2013).
- [29] G. A. Meehl, J. M. Arblaster, K. Matthes, F. Sassi, and H. van Loon, Amplifying the Pacific climate system response to a small 11-year solar cycle forcing, *Science* **325**, 1114 (2009).
- [30] T. H. Frame and L. J. Gray, The 11-yr solar cycle in ERA-40 data: an update to 2008, *J. Clim.* **23**, 2213 (2010).
- [31] M. Agostini, K. Altenmüller, S. Appel, V. Atroshchenko, Z. Bagdasarian, D. Basilico, G. Bellini, J. Benziger, D. Bick, I. Bolognino *et al.* (Borexino Collaboration), Modulation of the cosmic muon signal in ten years of Borexino data, *J. Cosmol. Astropart. Phys.* **2019**, 046 (2019).
- [32] H. Lu, M. A. Cliverd, A. Seppälä, and L. L. Hood, Geomagnetic perturbations on stratospheric circulation in late winter and spring, *J. Geophys. Res: Atmos* **113**, D16106 (2008).
- [33] A. Seppälä, H. Lu, M. A. Clilverd, and C. J. Rodger, Geomagnetic activity signatures in wintertime stratosphere wind, temperature, and wave response, *J. Geophys. Res: Atmos* **118**, 2169 (2013).
- [34] S. Osprey, J. Barnett, J. Smith, P. Adamson, C. Andreopoulos, K. E. Arms, R. Armstrong, D. J. Auty, D. S. Ayres, B. Baller *et al.*, Sudden stratospheric warmings seen in MINOS deep underground muon data, *Geophys. Res. Lett.* **36**, L05809 (2009).
- [35] R. Gelaro, W. McCarty, M. J. Suárez, R. Todling, A. Molod, L. Takacs, C. A. Randles, A. Darmenov, M. G. Bosilovich, R. Reichle *et al.*, The modern-era retrospective analysis for research and applications, version 2 (MERRA-2), *J. Clim.* **30**, 5419 (2017).
- [36] H. Hersbach, B. Bell, P. Berrisford, S. Hirahara, A. Horányi, J. Muñoz-Sabater, J. Nicolas, C. Peubey, R. Radu, D. Schepers *et al.*, The ERA5 global reanalysis, *Q. J. R. Meteorolog. Soc.* **146**, 1999 (2020).
- [37] P. Kumar and E. Foufoula-Georgiou, Wavelet analysis for geophysical applications, *Rev. Geophys* **35**, 385 (1997).
- [38] D. B. Percival and A. T. Walden, *Wavelet Methods for Time Series Analysis* (Cambridge University Press, Cambridge, 2006), Vol. 4.
- [39] C. Torrence and P. J. Webster, Interdecadal changes in the ENSO–monsoon system, *J. Clim.* **12**, 2679 (1999).
- [40] Freeware SSA-MTM Toolkit at <http://www.atmos.ucla.edu/tcd/ssa>.